Journal of Nuclear Materials 444 (2014) 237–246

Contents lists available at ScienceDirect

Journal of Nuclear Materials

journal homepage: www.elsevier.com/locate/jnucmat

Interaction of minor alloying elements of high-Cr ferritic steels with lattice defects: An *ab initio* study

A. Bakaev [a,b,c], D. Terentyev [a,*], G. Bonny [a], T.P.C. Klaver [d], P. Olsson [e], D. Van Neck [b]

[a] SCK·CEN, Nuclear Materials Science Institute, Boeretang 200, Mol B2400, Belgium
[b] Center for Molecular Modeling, Department of Physics and Astronomy, Ghent University, Technologiepark 903, 9052 Zwijnaarde, Belgium
[c] Department of Experimental Nuclear Physics K-89, Faculty of Physics and Mechanics, St. Petersburg State Polytechnical University, 29 Polytekhnicheskaya str., 195251 St. Petersburg, Russia
[d] Department of Materials Science and Engineering, Faculty of 3mE, TU Delft, Mekelweg 2, 2628 CD Delft, The Netherlands
[e] Department of Neutron Research, Angstrom Laboratory, Uppsala University, Box 525, SE-75120 Uppsala, Sweden

HIGHLIGHTS

- The interaction of Mo, W, Nb, Ta, V, Mn, Si with point and extended defects is characterized.
- Mn and Si exhibit peculiar interaction with both point and extended lattice defects.
- The results for substitutional atoms of the refractory metals well follow one specific trend.

ARTICLE INFO

Article history:
Received 23 August 2013
Accepted 26 September 2013
Available online 5 October 2013

ABSTRACT

Basic properties of minor alloying elements, namely Mo, W, Nb, Ta, V, Mn, Si entering the conventional and reduced-activation structural Fe–(9–12)Cr steels have been analyzed using *ab initio* calculations. The electronic structure calculations were applied to study the interaction of minor alloying elements with a number of important and well defined lattice structures, such as point defects, the $1/2\langle 1\,1\,1\rangle$ screw dislocation core, high angle symmetric grain boundaries and free surfaces. The studied elements were classified according to their similarities and discrepancies regarding the interaction with the above mentioned defects. The refractory alloying elements are found to follow the same trend whereas Mn and Si exhibit peculiar behavior with respect to the interaction with both point and extended lattice defects. The obtained results are discussed and compared with previously published *ab initio* and available experimental data.

1. Introduction

Because of its low price and superior mechanical properties, Fe-based alloys are one of the most important and widely used metallic materials. One of the fields of application for ferritic steels is the nuclear sector, which due to large safety margins poses special requirements such as good corrosion resistance, low creep rate, high mechanical yield stress and ductility [1,2]. It is important that these properties must be preserved upon exploitation in a radiation environment, which is known to cause the degradation of the desired materials properties [1]. The irradiation-induced degradation originates from out-of-equilibrium atomic rearrangement processes that occur by means of radiation induced defects, whose density is much higher than the thermal equilibrium vacancy concentration. Moreover, some of the lattice defects such as self-interstitial atoms (SIAs) and dislocation loops cannot be generated under thermal ageing conditions due to their very high formation energy.

Interstitial impurities and alloying elements (AEs) play a key role in the development of the materials with designed properties [1]. Consequently, the interaction of the steel's alloying elements with radiation defects, efficiency of their mass transport, affinity of the alloying elements to different microstructural units (e.g. grain boundary, free surface, dislocations, etc.) determine their rearrangement in the course of the irradiation process. For example, non-equilibrium segregation of solutes may lead to the formation of unwanted secondary phases or reduce the strength of grain boundaries [3]. Thus, the preservation of the optimum microstructure during high temperature irradiation is essential for the resistance against the degradation of the material's mechanical properties.

In an effort to study the properties of lattice defects at the atomic scale, a few density functional theory (DFT) works have already been devoted to characterize the interaction of the most important elements of ferritic–martensitic steels, i.e. C and Cr. In particular, DFT methods were applied to investigate the properties of point,

* Corresponding author. Tel.: +32 14333197.
E-mail address: dterenty@sckcen.be (D. Terentyev).

0022-3115/$ - see front matter © 2013 Elsevier B.V. All rights reserved.
http://dx.doi.org/10.1016/j.jnucmat.2013.09.053

Table 1
The type of periodicity, number of atoms, size of the crystal and *k*-point mesh of the studied configurations. The column 'additional information' reports the orientation and the type of the GBs and the orientation of free surfaces in the 2D slabs.

Configuration/purpose	Periodicity	Number of atoms	Size of the crystal, $a_0 \times a_0 \times a_0$	*K*-point mesh	Additional information
Bulk Fe calculations	3D	128	$4.0 \times 4.0 \times 4.0$	$3 \times 3 \times 3$	
Interaction of solute with GB	3D	72	$1.4 \times 2.4 \times 10.6$	$9 \times 5 \times 1$	$\Sigma3\langle110\rangle\{111\}$
		96	$2.8 \times 1.7 \times 9.9$	$7 \times 9 \times 1$	$\Sigma3\langle110\rangle\{112\}$
		120	$1.0 \times 3.2 \times 19.2$	$9 \times 5 \times 1$	$\Sigma5\langle100\rangle\{013\}$
Interaction of solute with free surfaces	2D	126	$3.0 \times 3.0 \times 10.5$	$5 \times 5 \times 1$	$\langle100\rangle$
		72	$12.0 \times 2{,}4 \times 1.7$	$1 \times 7 \times 9$	$\langle110\rangle$
		144	$4.2 \times 4.9 \times 7.0$	$3 \times 1 \times 1$	$\langle111\rangle$
		72	$2.8 \times 8.4 \times 2.6$	$5 \times 1 \times 6$	$\langle112\rangle$
Inter-row potential	3D	36	$4.2 \times 4.9 \times 0.9$	$3 \times 2 \times 9$	
Interaction of solute with a $1/2\langle111\rangle$ screw dislocation	1D	108	$10.0 \times 8.8 \times 0.9$	$1 \times 1 \times 12$	

linear and some planar defects in bcc Fe [4–9], FeC [10–13] and FeCr [14–17] systems. However, for the other minor alloying elements typically entering high-Cr commercial steels no extended study has been performed yet.

In this work we perform a DFT study considering the most important minor alloying elements entering the conventional structural (9–12)Cr steels (e.g. T91 and HT9) and reduced activation steels (e.g. E97 and F82H). Besides Cr and C, the minor alloying elements considered are [1]: Mo, W, Nb, Ta, V, Mn and Si. W and Mo act as ferrite stabilizers (as well as Si) and also contribute to solid solution hardening [18–21]. In addition, they may contribute to the formation of Laves phases (if the concentration exceeds ~1%) [20]. V, Nb and Ta are strong carbide formers [20]. Mn on the other hand is an austenite stabilizer used during the production process [22].

In this work, electronic structure calculations are performed to consider the interaction of these minor AEs with a number of important and well defined lattice structures, such as point defects, the core structure of a $1/2\langle111\rangle$ screw dislocation, high angle symmetric grain boundaries and free surfaces. As the first step we perform calculations in pure Fe matrix and introduce Cr in the dilute limit with the purpose to distinguish and separate contributions of AEs to different radiation-related degradation mechanisms. Additionally, the goal is to provide a full and consistent set of *ab initio* data to be used for the parameterization and validation of upper-scale atomistic cohesive models for large scale simulations. The correspondence between the obtained DFT data and available experimental data is also discussed.

2. Calculation details

2.1. General scheme

In this work, we have performed three types of *ab initio* calculations considering minor AEs in 3D-bulk, 2D-slabs with free surfaces and grain boundaries and 1D-periodic systems containing a $1/2\langle111\rangle$ screw dislocation. The settings of 3D-bulk calculations are described below, while the description of the model for 2D- and 1D-periodic samples is given in Section 2.3. The DFT calculations were performed using the Vienna *ab initio* Simulation Package VASP [23,24]. We used the projector-augmented wave potentials [25,26] for the calculation of the electronic ground state of the system. The electron exchange–correlation functional was described within the generalized gradient approximation using

Table 2
Ground state properties of the considered AEs. Excess pressure for 3D-periodic bcc Fe cell, containing 127 Fe atoms and one substitutional AE atom is reported in the last column of the table. The abbreviations NM and AFM stand for non-magnetic and antiferromagnetic states, respectively.

Atom	Ground-state structure	Lattice parameter, (Å)	Excess pressure, (kB)
W	Bcc NM	3.176	8.1
Mo	Bcc NM	3.157	7.8
Nb	Bcc NM	3.321	10.6
Ta	Bcc NM	3.312	9.7
V	Bcc NM	2.978	2.7
Mn	58 atoms, AFM	8.544	2.7
Si	Diamond NM	5.470	-0.1
Cr	Bcc AFM	2.849	2.7

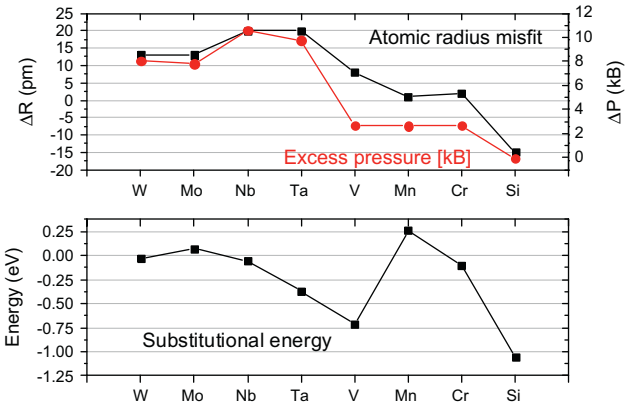

Fig. 1. The upper figure shows the atomic radius misfit (positive misfit means that atom is oversized as compared to equilibrium atomic volume of Fe) and excess pressure computed in the ionically relaxed systems (see text for details) containing a solute atom of the elements indicated. The lower figure shows the substitutional energy.

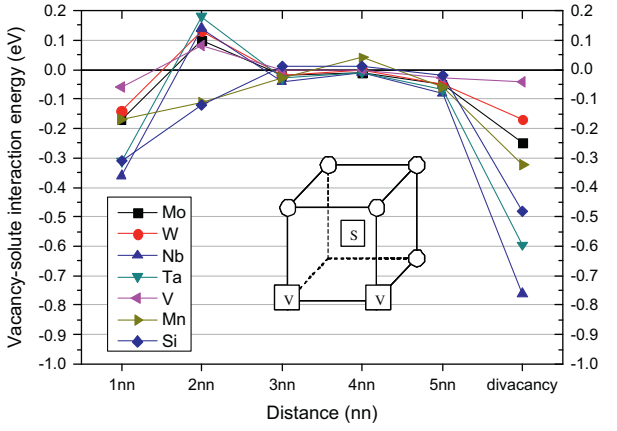

Fig. 2. Vacancy-solute interaction energy as a function of distance. The last value is the total binding energy for the most stable (for all studied alloying elements) divacancy – solute complex. The structure of the complex is shown in an inset figure.

PW91 functional [27], with a Vosko–Wilk–Nusair interpolation [28]. For Fe, Cr, Mo, W, Nb, Ta, V, Mn and Si pseudo potentials with 8, 6, 6, 6, 11, 5, 5, 7 and 4 valence electrons were used, respectively. The selected potential for Nb treats the 4p semi-core states as valence states.

Ionic relaxation was performed using the generalized gradient approximation with a force convergence criterion of 0.03 eV/Å. All the calculations were performed keeping the cell shape and volume (equal to the equilibrium volume of bulk iron) constant unless other conditions are specified. The energy cutoff for calculations was 300 eV which was proven to be large enough to provide converged results [29]. A $3 \times 3 \times 3$ k-point mesh was sampled by the Monkhorst and Pack scheme for systems with 128 atoms. The lattice parameter of pure ferromagnetic Fe is taken to be 2.831 Å following previous studies [17,29]. It has been confirmed that this lattice parameter provides the lowest total energy for BCC Fe crystal.

The excess pressure of the single solute atom configurations was calculated as the difference between the external pressure (reported in the VASP output) of the system with and without the substitutional solute.

Given that we perform spin-polarized calculations in the ferromagnetic system and introduce anti-ferromagnetic impurities, one needs to be careful when selecting the initial value of the magnetic moment to ensure that the true minimum energy configuration is obtained after relaxation. In the case of calculations with Mn when its magnetic spin was not anti-ferromagnetic to Fe after the relaxation, we performed additional calculations varying the absolute value of the initial moment as some of the results turned out to be particularly sensitive to the selection of the initial magnetic moment. In the paper we report the results corresponding to the lowest energy configurations only.

2.2. Substitutional and Interaction energy

To assess the substitution and interaction energy we apply standard definitions conventionally used in many similar DFT works [9]. The substitutional energy E_{sub} of a foreign atom F in the bcc Fe matrix is defined as:

$$E_{sub} = E(n\mathrm{Fe} + 1F) - \frac{n}{n+1} \times E((n+1)\mathrm{Fe}) - E(F)_{cryst}, \quad (1)$$

where $E(n\mathrm{Fe} + 1F)$ is the energy of a crystal containing n Fe atoms and one foreign atom, $E((n+1)\mathrm{Fe})$ is the energy of the pure Fe crystal with the same size as the former one, and $E(F)_{cryst}$ is the energy per atom of the element F in its most stable phase.

The interaction energy of n defects $\{A_i\}$ is defined as [9]:

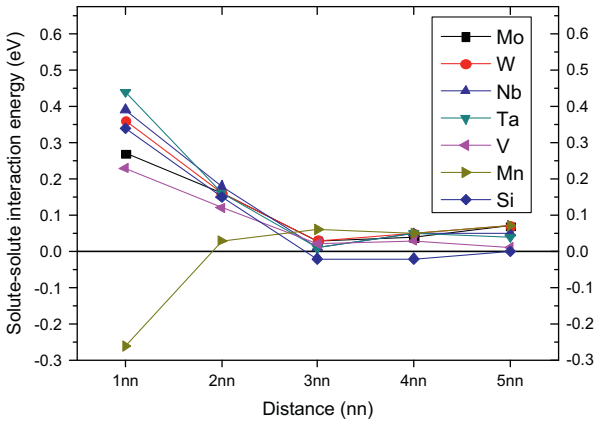

Fig. 3. Solute–solute interaction energy as a function of distance.

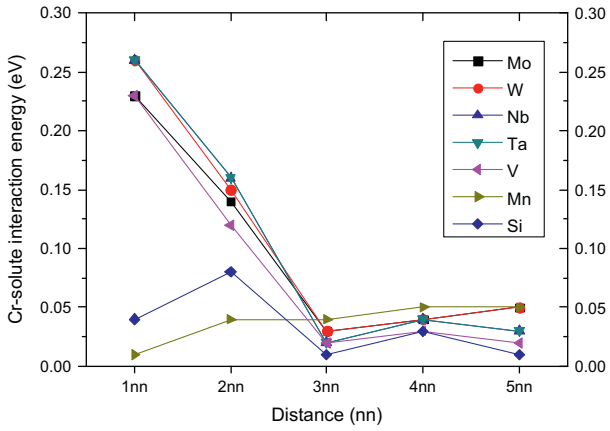

Fig. 4. Cr-solute interaction energy as a function of distance.

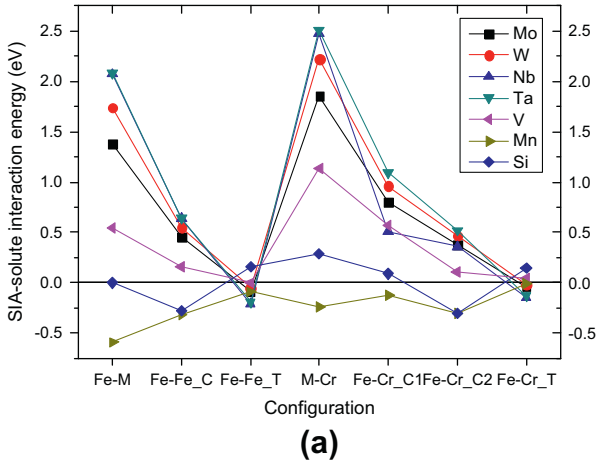

Fig. 5. (a) SIA-solute interaction energy as a function of local arrangement. (b) Schematic figure explaining the considered configurations. M: Fe-solute mixed dumbbell; C1 and C2 are the sites located in the compressive region of the dumbbell strain field; T is the site located in the tensile region of the dumbbell strain field. Configurations denoted on the figure as Fe–Cr_C/T correspond to the interaction of the mixed Fe–Cr dumbbell with another solute atom placed in either tensile or compressive site. Note that there are two non-equivalent compressive sites. M–Cr configuration corresponds to the case when the dumbbell is formed by Cr and another solute atom. In the case of the configurations involving Cr atom in the dumbbell, the interaction energy between the Fe–Cr dumbbell and another solute atom is calculated.

$$E_i(\{A_i\}) = [E(\{A_i\}) + (n-1)E_0] - \left[\sum_{i=1}^{n} E(A_i)\right], \quad (2)$$

where $E(A_i)$ is the energy of the configuration containing A_i only, $E(\{A_i\})$ is the energy of the configuration with all the n defects, and E_0 refers to a configuration containing no defects or impurities, i.e. bulk bcc iron. Following this notation, a negative value implies an attractive interaction and vice versa.

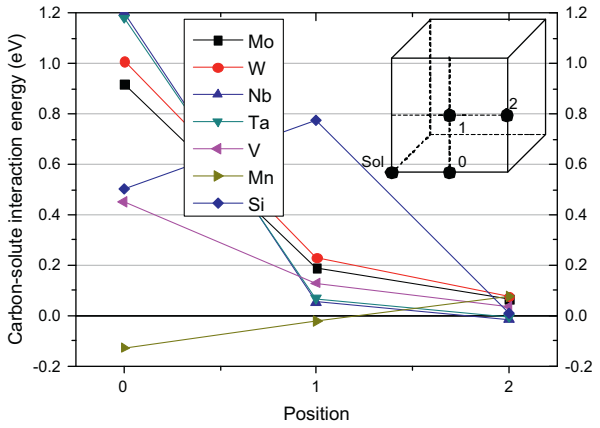

Fig. 6. Interaction energy between an interstitial carbon atom and substitutional solute measured in the positions schematically shown on the inset figure.

2.3. Calculations in 2D- and 1D-periodic cells

2D- and 1D-periodic cells were used to characterize the interaction of minor alloying impurities (as substitutional atoms at the Fe sites) with free surfaces, grain boundaries and the core of a 1/2⟨111⟩ screw dislocation. The specific DFT settings for each considered supercell are provided in Table 1. The reported *k*-point meshes were tested to provide converged results. In the 2D-periodic cells containing free surfaces, the width of vacuum was set to 10 Å, which was verified to be large enough to avoid interaction between free surfaces through the periodic boundaries. Prior to introducing an impurity, the dimensions of supercells containing grain boundaries were established by optimizing the spacing normal to a grain boundary (GB) interface to ensure the minimum energy.

To compare different grain boundaries we use the following parameters: (a) the GB energy (γ_{GB}) which is defined as [8]:

$$\gamma_{GB} = \frac{E_{GB} - E_{SC}}{2A}, \tag{3}$$

where E_{GB} and E_{SC} are the energies of the GB supercell and its corresponding single total crystal, respectively. A stands for the area of the GB plane. The corresponding single crystal (without GB) was obtained keeping the same basis orientation, *k*-point mesh and cut-off energy. The free surface energy (γ_{FS}) is defined in a similar way, where E_{GB} is substituted by the total energy of the crystal with free surfaces E_{FS}, and A is the free surface area.

(b). The GB excess free volume (Ω) is defined as [8];

$$\Omega = \frac{V_{GB} - V_{SC}}{2A}, \tag{4}$$

where V_{GB} and V_{SC} stand for the volumes of the GB supercell and its corresponding single crystal with the same number of atoms, respectively. A is the grain boundary interface area.

Table 3
Characteristics of free surfaces as obtained by DFT calculations.

Surface orientation	Surface area (a_0^2)	Number of atoms on the surface layer	Surface energy (J/m^2)	Magnetic moment of the atoms (Fe/single Mn) on the top layer (μ_B)	Number of non-equivalent planes along *Z*-direction
100	9.0	9	2.52	2.9/−3.6	7
110	4.2	6	2.44	2.6/−3.2	6
111	20.8	12	2.67	2.8/−3.5	6
112	7.4	6	2.58	2.7/−3.4	6

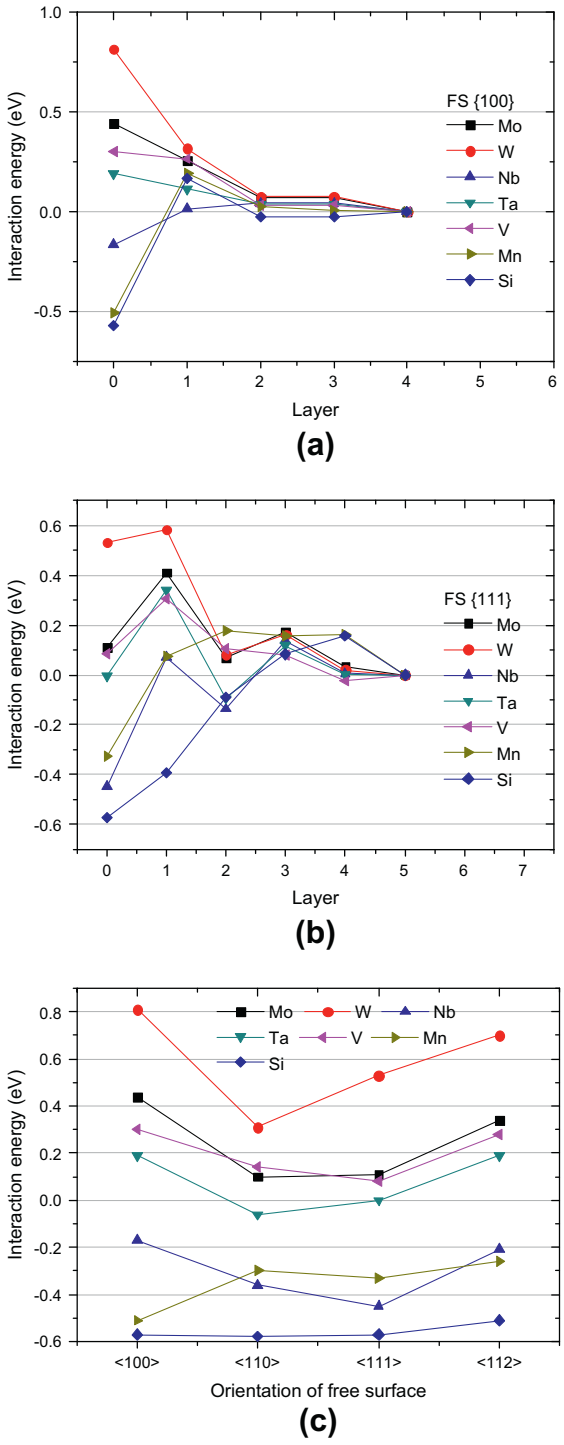

Fig. 7. Interaction energy of substitutional solutes with free surfaces. (a) As a function of depth for the FS with {100} orientation; (b) as a function of depth for the FS with {111} orientation; (c) for all the studied orientations for the case of a solute being placed in the top layer of the surface.

3. Results

3.1. Interaction with point defects

We start with the description of the properties of substitutional atoms. The majority (except for Si) of the calculations of this section had already been performed in the work [9]. We enhance the results of that work by adding excess pressure analysis,

studying interactions with carbon and refining the calculations with Mn. Table 2 reports the used reference structures of the considered AEs. The atomic radius misfit and excess pressure are given in the upper bar of Fig. 1. We see that there is a good correspondence between the calculated excess pressure and atomic size misfit. The largest lattice expansion is realized for the solutes representing refractory metals, i.e. Mo, W, Ta and Nb. It is somewhat smaller for V, Mn and Cr, and is about zero for the semi-conductor Si.

The substitutional energy for each considered AE is presented in the lower part of Fig. 1. The smallest substitutional energy (about zero) is obtained for the refractory metals, except for Ta whose substitution causes an exothermic reaction and the released heat is 0.37 eV. Strongly negative substitutional energies are found for V and Si, −0.71 and −1.06 eV respectively. And finally, Mn has a well pronounced positive substitution energy.

The interaction energy between a vacancy and the solutes is given in Fig. 2 as a function of distance, expressed in nearest neighbor (nn) distance units. Irrespective of the solute type, all the species are attracted to a vacancy in the first nearest neighbor (1nn) position, and the interaction becomes negligible once the objects are placed further than 2nn distance. Considering the short range interaction (i.e. in the 1nn and 2nn), the studied elements can be subdivided into two types. Mn and Si exhibit attractive interaction with a vacancy in both 1nn and 2nn position, and therefore these elements might potentially be dragged by a vacancy [30], although detailed analysis of the migration barriers within five-frequency model is required for a definitive conclusion. All other studied elements exhibit repulsive interaction in 2nn position and attractive in the 1nn. This indicates that these AEs should act as short-range traps for vacancies.

A number of remarks can be made regarding the absolute value of the interaction energy in 1nn position. For the refractory elements and vanadium, the interaction energy rises consistently with the size misfit factor. In contrast, Si and Mn exhibit much stronger binding than expected from the lattice strain induced in perfect bcc Fe. For completeness, we also computed the interaction energy between the di-vacancy and a solute (2nn vacancy–vacancy complex which is the most stable in Fe and solute at 1nn). For all tested elements the interaction is found to be strongly attractive, except for vanadium (see Fig. 2).

Next we proceed to the solute–solute and solute-Cr interactions, which are presented in Figs. 3 and 4, respectively. As in the case of the interaction with a vacancy, the interaction is limited to 1nn and 2nn distance. Among the considered elements, Mn and Si are again the outstanding ones. Indeed, all the solutes exhibit strong mutual repulsion in Fe and repulsion from substitutional Cr, except for the Mn–Mn pair, for which a considerable binding (−0.26 eV) is predicted. This binding, however, changes to weak repulsion in the 2nn and 3nn positions. Why the strong repulsion, found for Cr–Cr pairs in Fe, does not occur for Mn–Mn pair will be discussed later. Although Si and Mn also exhibit weak repulsive interaction with Cr in the immediate neighborhood, its absolute value is much lower than for the other elements.

The interaction energy between $a\langle 1\,1\,0\rangle$ dumbbell (the most stable SIA configuration in Fe) and different solutes is presented in Fig. 5(a) for different local arrangements. The figure caption explains atomic arrangement for the different configurations and Fig. 5(b) schematically shows these arrangements. All the transition metals, except for Mn, exhibit repulsive interaction if placed in the compressive (C) site, attractive interaction in the tensile site (T), and none of them except Mn form stable Fe-solute or Cr-solute dumbbells. The repulsive interaction in the compressive site and the inability to form mixed dumbbell is consistent with the oversized nature of W, Mo, Ta, Nb, V (as substitutes in Fe matrix, see Fig. 1). The attractive interaction in the tensile site is also consistent with expectations from elasticity theory consideration. Finally, given that Cr also behaves as an oversized substitutional, a stable Cr-solute dumbbell does not form with any considered refractory metals nor vanadium atom. Mn shows attractive interaction in

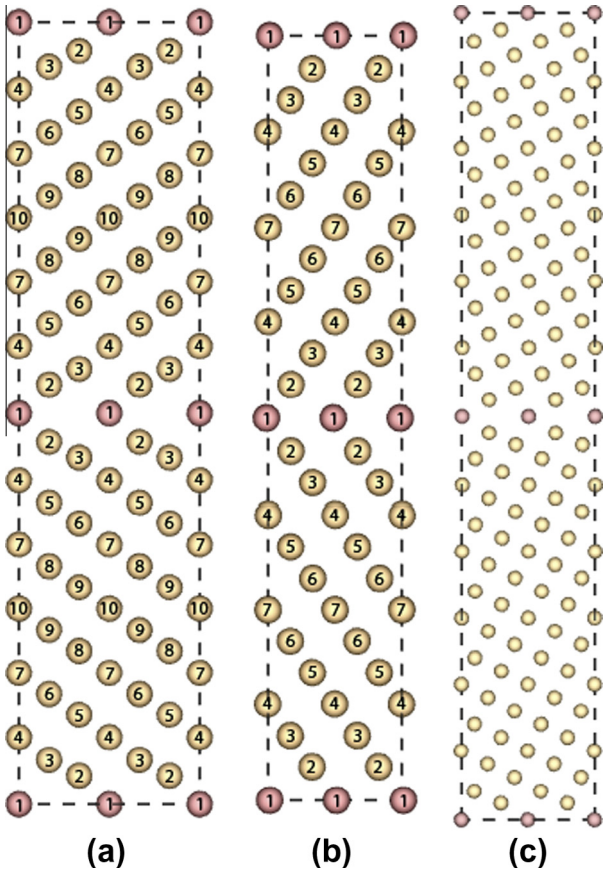

Fig. 8. YZ-plane views of three grain boundaries (a: $\Sigma 3\langle 1\,1\,0\rangle\{1\,1\,1\}$, b: $\Sigma 3\langle 1\,1\,0\rangle\{1\,1\,2\}$, c: $\Sigma 5\langle 1\,0\,0\rangle\{0\,1\,3\}$). In (a) and (b) the equivalent lattice sites are marked with the same numbers. The dark colored atoms represent the grain boundary.

Table 4
Characteristics of grain boundaries as obtained by DFT calculations here.

GB type, XYZ orientation of the crystal	GB area, (a_0^2)	Number of atoms on the GB layer	Number of non-equivalent planes along Z-direction within one grain	GB energy γ_{GB} (J/m^2)	GB excess free volume (Ω), (Å)
$\Sigma 3\langle 1\,1\,0\rangle\{1\,1\,1\}$ $[1\,1\,0]\times[1\,\bar{1}\,1]\times[\bar{1}\,1\,2]$	3.46	2	10	−1.56	0.11
$\Sigma 3\langle 1\,1\,0\rangle\{1\,1\,2\}[1\,1\,0]\times[\bar{1}\,1\,2]\times[1\,\bar{1}\,1]$	4.90	4	7	−0.47	0.04
$\Sigma 5\langle 1\,0\,0\rangle\{0\,1\,3\}[1\,0\,0]\times[0\,1\,3]\times[0\,\bar{3}\,1]$	3.16	2	10	−1.51	0.11

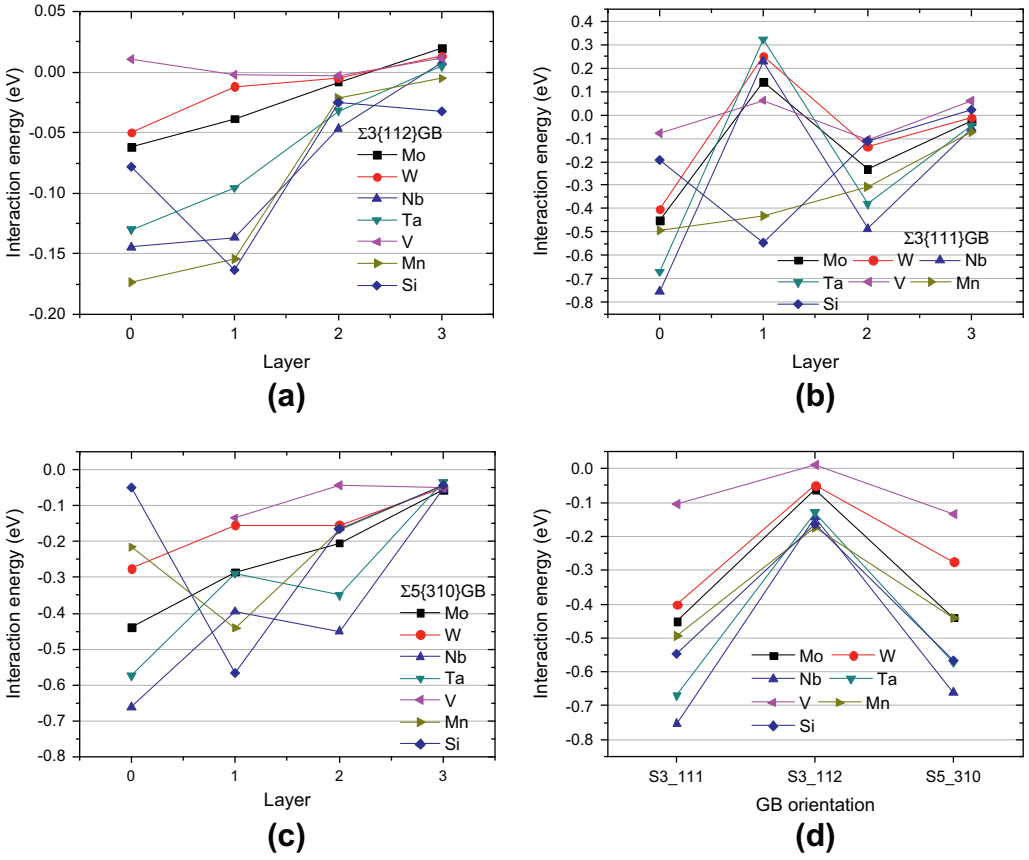

Fig. 9. Interaction energy of substitutional solutes with the three different grain boundaries (a: $\Sigma3\langle110\rangle\{112\}$, b: $\Sigma3\langle110\rangle\{111\}$, c: $\Sigma5\langle001\rangle\{310\}$) computed for the four layers near the grain boundary interface. Figure d presents the maximum interaction energy as a function of GB orientation.

all the studied configurations with dumbbells except for being in tensile sites near to Fe–Fe and Fe–Cr dumbbells where the interaction is very weak or zero, respectively. The reasons for the peculiar behavior of Mn will be discussed later in Section 4. Finally, Si repels or shows negligible interaction in all the configurations except for attraction to Fe–Fe dumbbell in the compressive site as well as to the mixed Fe–Cr dumbbell in the compressive site C2 (see Fig. 5b), i.e. when the distance between Si and Cr is almost as large as 3nn so that their repulsion is negligible (see Fig. 4).

Fig. 6 displays the interaction energy between an interstitial carbon atom in an octahedral position (the most stable configuration [31]) and a substitutional solute atom, calculated in the positions schematically shown in the inset figure. The interaction between an interstitial carbon and all the studied elements is repulsive except for Mn, to which the carbon atom is attracted in the closest octahedral position. The carbon-solute repulsion vanishes at the distance of $a_0\sqrt{(5/2)}$.

3.2. Interaction with interfaces

Four different open surfaces were considered in this work, namely {100}, {111}, {110} and {112}. The latter two (in addition to {123}) are known to be primary dislocation glide planes in bcc metals, while {100} and {111} are close packed surface planes. The sizes of the supercells used to compute the interaction energy are given in Table 3.

The interaction with the free surface in all the cases was found to last approximately up to the 3rd or 4th interatomic layer. However, the strongest interaction, no matter if it was attractive or repulsive, was seen to take place at the top layer in most of the cases. Only three exceptions were identified for Mo, V and Ta interacting with a {111} surface (see Fig. 7a and b presenting the interaction energy as a function of depth for the FSs with {100} and {111} orientations, respectively). In the following we discuss only the interaction energy for the top layer, see Fig. 7c. Nb, Mn and Si are attracted to all the considered surfaces whereas W, Mo and V exhibit repulsive interaction. Ta exhibits almost no interaction with {110} and {111} surfaces, and weak repulsion from {100} and {112} surfaces is predicted.

The considered grain boundary interfaces have different dimensions, depending on the GB type. To give an idea how close the periodical in-plane images of the alloying atom are, we report the distance in Table 4 together with the interface area and other data for each GB studied such as GB energy and GB excess free volume. The side views (YZ plane) of the studied GB are shown in Fig. 8. The calculated values of the GB energies are in good agreement with the previously published *ab initio* results [8].

As in the case of the free surfaces, the interaction energy was seen to vary only a few (three in most of the cases) interatomic layers, close to the interface plane. This time, however, the variation of the interaction energy is not monotonic and therefore we present the computed interaction energy as a function of location of the solute with respect to the grain boundary plane (GBP), shown in Fig. 9. In all the cases, the considered solutes were found to be attracted to the studied GBs except for vanadium which does not interact with grain boundary $\Sigma3\langle110\rangle\{112\}$. Note that the binding with a $\Sigma3\langle110\rangle\{112\}$ GB was much weaker (by about a factor of three) than with the other two GBs, i.e. $\Sigma3\langle110\rangle\{111\}$ and $\Sigma5\langle100\rangle\{013\}$. It is also seen from the figures that the profiles of the interaction energy for the refractory metals have similar

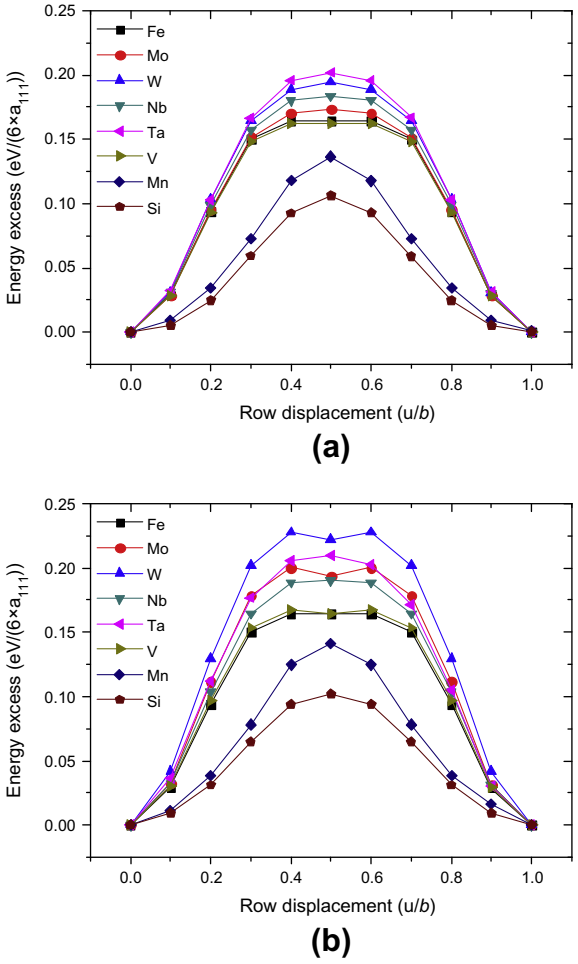

Fig. 10. The variation of the excess energy (normalized over a length of the displaced row and the amount of nearest-neighbor atomic rows (six rows)) versus atomic row displacement ($u/\boldsymbol{b}$) for: (a) a single row of solutes in the Fe matrix; (b) a row of solutes dragged next to another row of solutes (of the same type).

shapes, although their absolute values differ. Si and Mn solutes, on the other hand, exhibit somewhat irregular behavior. For instance, the strongest interaction for Si with all studied GB occurs in the 1st layer away from the GBP, whereas all other elements are mostly attracted to the GB interface itself. Note that in the $\Sigma3\langle110\rangle\{111\}$GB all the solutes except for Mn and Si show repulsive interaction at the 1st layer from the GBP whereas Mn and Si are attracted to the GB.

The maximum binding energy between the considered solutes and GBs is presented in Fig. 9d. We observe that almost irrespective of the GB orientation the order at which the binding energy increases is as follows: V, (W & Mo), (Mn, Si, Ta & Nb). This trend is especially easy to observe in the case of high-energy GBs such as $\Sigma3\langle110\rangle\{111\}$ and $\Sigma5\langle100\rangle\{013\}$. The strongest interaction of Ta and Nb is most likely related to the fact that these solutes produce the largest strain (see Fig. 1), which can be partially relieved at the GB interface. Correspondingly, the smallest binding energy found for vanadium can also be attributed to its small excess pressure generated in bulk bcc Fe (see Fig. 1). The relatively strong binding energy found for Mn and Si (for the $\Sigma3\langle110\rangle\{111\}$ GB) cannot be simply explained by the relief of the lattice strain. Finding the reasons for peculiar behavior of Mn and Si requires in-depth investigation and understanding of the modification of the magnetic state and directional bonding arrangement, which will be a subject of a separate work.

3.3. Interaction with a screw dislocation and lattice friction

As mentioned in the introduction, we also perform calculations to investigate the influence of the solutes on the core structure of a $1/2\langle111\rangle$ screw dislocation and slip-resistance of a $\langle111\rangle$ atomic row (a.k.a. interatomic row potential). The atomic row (AR) method accounts for the relaxation between $\langle111\rangle$ atomic strings and the inter-row potential derived directly from DFT calculations correlates with the type of core structure of a $1/2\langle111\rangle$ screw dislocation [32], which may be isotropic or degenerate [33] depending on the double hump or single hump shape of the interatomic row potential, respectively. In the cases when the flat top-structure is observed, the core configuration can be either degenerate or isotropic [32]. By computing the interatomic row potentials for solutes or pairs of solutes one clarifies the impact of solute-matrix and solute–solute interaction on the lattice friction against the slip involving sliding (re-arrangement) of $\langle111\rangle$ atomic rows. The latter process corresponds to the glide of a $1/2\langle111\rangle$ screw dislocation in bcc metals.

The variation of the energy (normalized over a length of the displaced row and the amount of nearest-neighbor atomic rows (six rows)) versus atomic row displacement ($u/\boldsymbol{b}$) for a single row of solute atoms in the Fe matrix and for a row of solutes standing next to another row of solutes (of the same type) is given in Fig. 10 a and b, respectively. Fig. 10a shows that the addition of an isolated row of oversized refractory metals causes an increase of the amplitude of the energy excess by a factor 1.05–1.25, suggesting that they should suppress the glide of $\langle111\rangle$ rows. The presence of a vanadium row, on the other hand, hardly changes the interatomic potential profile. Mn and Si clearly decrease the atomic row shift resistance and in addition change the shape of the profiles from a double-hump-like or flat-top to a sinusoidal one (single hump). This should be also reflected in the core structure of the screw dislocation, as was validated by separate DFT calculations presented in the following. Fig. 10b, which represents the solute–solute row interatomic potential, essentially shows that only refractory metals cause enhancement of the inter-row friction, while pairs of Mn and Si rows exhibit a weaker friction than between Fe rows and V causes no change of friction.

The differential displacement maps for the studied AEs in different positions relative to the dislocation core structure are presented in Fig. 11. In pure bcc Fe, a $1/2\langle111\rangle$ screw dislocation has a compact non-degenerate core structure. Three $\langle111\rangle$ rows form the core of the screw dislocation. Addition of Mo, Nb, Mn, Ta, V or W in the core position does not disturb the equilibrium structure of the core, which remains symmetric and non-degenerate as shown for Mo in cell Mo-Core in Fig. 11. By displacing Mo (or Nb, Mn, Ta, V, W) away from the core (see cells Mo-1nn and Mo-2nn), its structure remains unchanged, although some limited distortion occurs in the immediate vicinity of an introduced solute. Si clearly modifies the core structure making it extended (split) in a $\{110\}$ plane (see Fig. 11, cell Si-Core). The orientation of the split plane depends on the particular position of Si in the core. The core also remains extended if Si is placed in the 1st nn position (see Fig. 11, cell Si-1nn). Recovery of the symmetric non-degenerate core structure occurs if Si is placed in the 2nd nn position (see Fig. 11 cell Si-2nn).

A similar effect as for Si on the core extension in a $\{110\}$ plane is seen for W, Ta, Nb and weakly for Mo being placed in the 1nn position. Thus, these essentially oversized elements affect the core structure while the dislocation approaches them. Finally, a Mn atom placed at the 1nn position causes heavy relaxation of the dislocation core so that its actual position displaces towards the solute, as shown in cell Mn-1nn of Fig. 11.

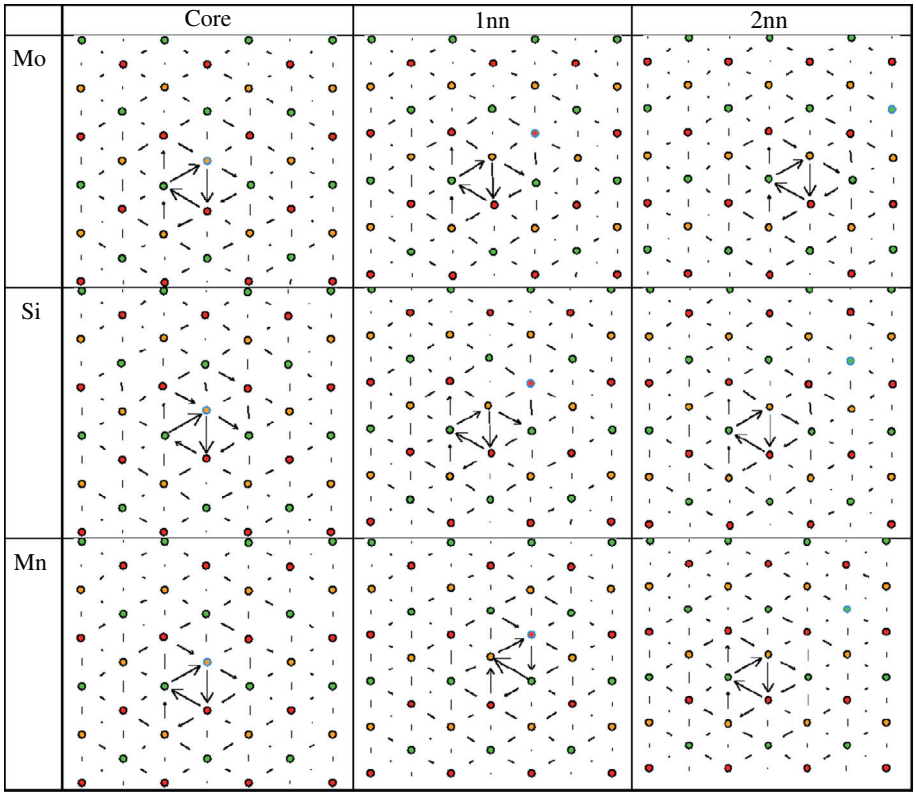

Fig. 11. Differential displacement maps for a 1/2⟨1 1 1⟩ screw dislocation interacting with solutes calculated after full relaxation. The alloying element (specified in the left column) is shown by a blue circle. Three different positions for AE are considered, namely: in-core and 1st and 2nd nearest neighbor from the core.

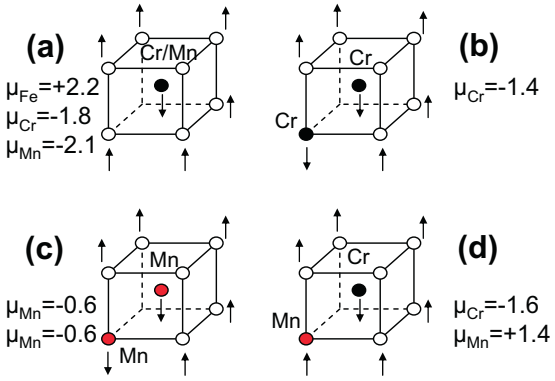

Fig. 12. Magnetic moments obtained for Fe, Cr and Mn atoms for different atomic configurations, namely: (a) one substitutional atom, (b) 1nn pair of Cr atoms, (c) 1nn pair of Mn atoms, (d) 1nn Mn–Cr pair.

4. Summary and conclusions

One of the most striking features of Mn is the absence of Mn–Mn repulsion at the 1nn distance, which is predicted for all the other elements. The reason for this absence could provide an explanation for other deviations from patterns that were observed. Mn behaves as anti-ferromagnetic (its spin is opposite to the spins of Fe atoms) in bcc Fe and the repulsion between Mn atoms would be natural due to the expected 'frustration' of magnetic moments, which was discovered earlier for a pair of Cr atoms in Fe [34]. Yet, it is predicted that two Mn atoms attract each other yielding an interaction energy of −0.26 eV. To rationalize the obtained result we have computed the magnetic moments on Mn and the surrounding Fe atoms in different atomic configurations, see Fig. 12. Given the above mentioned analogy with Cr, we repeated the same calculations for Cr to reveal the difference. For an isolated substitutional Mn/Cr atom its moment is anti-aligned to Fe atoms (see Fig. 12a) as expected. The moments on two Cr atoms placed as 1nn and relaxed (see Fig. 12b) are also anti-aligned with respect to the moments of Fe atoms, but the total value is now reduced to $-1.4\ \mu_B$ compared to $-1.8\ \mu_B$ for the isolated atom. In the case of the Mn–Mn pair, the magnetic moment on each Mn atom is strongly reduced to $-0.6\ \mu_B$, as shown in Fig. 12c. In the case of the Mn–Cr pair, for which the repulsion is also expected, the moment of the Mn atom is flipped to align with Fe atoms and there is apparently no opposition of magnetic moments (unlike in the case of Cr–Cr pair) and consequently no repulsion. Hence, the flexibility of the magnetic moment of the Mn atom and the ability of Mn to modify magnetic moments of the neibourhood Fe atoms are likely to be the key features explaining the absence of Mn–Mn and Mn–Cr repulsion as well as the moderate attraction of Mn to a pure Fe–Fe and mixed Fe–Cr⟨1 1 0⟩ dumbbell (see Fig. 5a). As a result, Mn is the only element among the studied ones which exhibits both remarkable attraction to an SIA and vacancy, and forms a stable mixed dumbbell at the same time, following the results obtained here.

For completeness, we bring to the reader's attention DFT and experimental data on Mn–Mn interaction. Mössbauer experiments on Fe5%Mn alloys performed by Chojcan et al. [35] deduced a repulsive interaction of 0.11–0.14 eV for Mn–Mn pairs of solute atoms. These values, however, are obtained assuming a binomial distribution of the Mn atoms which was not certain in that experiment since the solubility of Mn is less than 5% [36] in alpha Fe. Therefore it is unclear if comparison of the latter results with our DFT data is justified.

Vincent et al. [37] performed DFT calculations using ultrasoft pseudopotentials which show a repulsive interaction between

Mn–Mn pairs of 0.28 eV and 0.15 eV for 1nn and 2nn pairs, respectively. Beside the usage of another set of pseudopotentials, the difference with our results might be attributed to the different relaxation conditions.

The interaction of V–V pairs was studied in [35] and a negligible binding of about −0.01 to 0.01 eV was calculated. The DFT results obtained here predict a higher repulsive interaction of 0.23 eV for 1nn and 0.12 eV for 2nn. The later obtained experimental results by Chojcan in Fe–3%V [38] revealed repulsion of about 0.05 eV for V–V pairs. Therefore there is a qualitative agreement between our results and experimental data.

Our next point of the discussion is the correspondence between the predicted interaction nature of the solutes with point defects and available experimental evidence. The predicted strong attractive interaction for the Si-vacancy agrees well with the results of Nagai [39] and Möslang [40], suggesting the formation of stable vacancy-Si pairs. In the same experimental work, Möslang et al. could not reveal strong attractive interaction for a vacancy with Cr and Mn. Cr is indeed known to exhibit a very small positive binding energy with a vacancy (~0.05 eV). Mn, according to the utilized DFT method, is predicted to exhibit a non-negligible positive binding energy ([9] and present work). In addition, according to the resistivity recovery studies of e^- irradiated Fe–Mn alloys, Mn binds vacancies [41].

Considering the interaction with an SIA, the amount of experimental data is also rather limited. Mo is known to suppress the migration of Fe–Fe SIAs and thus acts as a trap for SIAs [42]. The trapping energy was determined to be about 0.06 eV, which is however about the uncertainty of the present calculations due to the limited supercell size. At the same time, Mo does not form the mixed dumbbell [42]. All these features are in line with the currently obtained results, and the binding energy for Mo in the tensile site of an Fe–Fe dumbbell is 0.08 eV in excellent agreement with the experimental result.

Si atoms also show suppression of long-range migration of SIAs (suppression of stage I_E) with increasing Si concentration in isochronal recovery experiments [43]. This has been interpreted as a multiple trapping effect, implying that trapped SIAs, instead of detrapping, may form mixed migrating dumbbells and then be bound to a second Si atom [43]. According to the present calculations Si acts as a relatively strong trap for Fe–Fe dumbbells (0.28 eV) and given the possible formation of mixed Si–Fe dumbbells, multiple trapping by Si is not excluded by our results.

Mn forms a stable mixed dumbbell [41], which agrees with the results of our calculations.

A number of results inconsistent with the trends obtained for refractory metals was obtained for anti-ferromagnetic Mn and diamagnetic Si. Below, we list the observed irregularities for Si and Mn:

1. Attractive interaction with a vacancy in both 1nn and 2nn position.
2. Considerable attractive interaction between two substitutional Mn atoms in the 1nn position.
3. No repulsive interaction with substitutional Cr.
4. Mn is the only element which form a stable mixed⟨1 1 0⟩ Fe–Mn dumbbell, with Si being neutral, while all the other considered elements exhibit strong repulsion.
5. Non-negligible attractive interaction with a ⟨1 1 0⟩ Fe–Fe dumbbell in the compressive site.
6. Mn is the only element which exhibits weak attractive interaction with an interstitial carbon.
7. Si, Mn (and Nb) exhibit considerable affinity to a free surface, in contrast to the other elements.
8. Mn and Si are the only elements which are found to facilitate ⟨1 1 1⟩ atomic row exchange.
9. Si is the only element that causes strong distortion of the core structure of a 1/2⟨1 1 1⟩ screw dislocation.

On other hand, all the considered refractory metals and vanadium, are characterized by the following features:

1. Moderate attraction with a vacancy in the 1nn and non-negligible repulsion in the 2nn.
2. Strong repulsion with Cr and with itself in the 1nn position.
3. Do not form a solute-Fe or solute-Cr⟨1 1 0⟩ dumbbell.
4. Strong repulsion from an isolated interstitial carbon.
5. No affinity to the free surface (except for Nb and Ta).
6. Moderate attraction to the GB interface, correlating with the size misfit factor.
7. Enhancement (except for V where no change is calculated) of the lattice friction that makes ⟨1 1 1⟩ atomic row exchange more difficult.
8. Do not alter the screw dislocation core structure if placed in the core, and do create expansion of the core in a {1 1 0} plane if the solute is placed at the 1nn position from the core.

Rationalization and understanding of the observed systematic trends and some off-trend results (specifically of Mn and Si) require further in-depth analysis.

Acknowledgements

This work was performed in the framework of the EFDA project. We are grateful to the ICT Department of Ghent University for partial support of this work. Part of calculations has been performed at HPC Julich within the 'SORT' project. The research was partly supported by the FWO grant.

References

[1] R.L. Klueh, A.T. Nelson, J. Nucl. Mater. 371 (2007) 37–52.
[2] O. Anderoglu, T. Byun, M. Toloczko, S. Maloy, Metall. Mater. Trans. A 44 (2013) 70–83.
[3] J.P. Wharry, Z. Jiao, V. Shankar, J.T. Busby, G.S. Was, J. Nucl. Mater. 417 (2011) 140–144.
[4] E. Vincent, C.S. Becquart, C. Domain, J. Nucl. Mater. 359 (2006) 227–237.
[5] E. Vincent, C.S. Becquart, C. Domain, Instrum. Methods B 228 (2005) 137–141.
[6] M. Itakura, H. Kaburaki, M. Yamaguchi, Acta Mater. 60 (2012) 3698–3710.
[7] D. Terentyev, T. Klaver, P. Olsson, M. Marinica, F. Willaime, C. Domain, L. Malerba, Phys. Rev. Lett. 100 (2008) 145503.
[8] S.K. Bhattacharya, S. Tanaka, Y. Shiihara, M. Kohyama, J. Phys.: Condens. Matter 25 (2013) 135004.
[9] P. Olsson, T.P.C. Klaver, C. Domain, Phys. Rev. B 81 (2010) 054102.
[10] C.S. Becquart, J.M. Raulot, G. Bencteux, C. Domain, M. Perez, S. Garruchet, H. Nguyen, Comput. Mater. Sci. 40 (2007) 119–129.
[11] C.C. Fu, E. Meslin, A. Barbu, F. Willaime, V. Oison, Effect of C on vacancy migration in alpha-iron symposium on theory, Modeling and Numerical Simulation of Multi-Physics Materials Behavior held at the 2007 MRS Fall Meeting Boston, MA, 2007, pp. 157–164.
[12] C.J. Forst, J. Slycke, K.J. Van Vliet, S. Yip, Phys. Rev. Lett. 96 (2006) 175501.
[13] C. Domain, C. Becquart, J. Foct, Phys. Rev. B 69 (2004) 144112.
[14] P. Olsson, I.A. Abrikosov, L. Vitos, J. Wallenius, J. Nucl. Mater. 321 (2003) 84–90.
[15] D. Nguyen-Manh, M.Y. Lavrentiev, S.L. Dudarev, J. Nucl. Mater. 386–388 (2009) 60–63.
[16] K.O.E. Henriksson, N. Sandberg, J. Wallenius, Appl. Phys. Lett. 93 (2008) 191912.
[17] T. Klaver, P. Olsson, M. Finnis, Phys. Rev. B 76 (2007) 214110.
[18] W.C. Leslie, Metall. Trans. 3 (1972) 5–26.
[19] J. Nutting, The structural stability of low alloy steels for power generation applications, Iom Communications Ltd., London, 1999.
[20] V.Z.K. Foldyna, V. Vodarek, J. Purmensky, 3rd EPRI Conference on Advanced Materials Technology for Fossil Plants, 2001, pp. 89–98.
[21] R.W.K. Honeycomb, Steels: Microstructure and Properties, Edward Arnold, London, 1981.
[22] M. Kutz, Handbook of Materials Selection, Wiley, New York, 2002.
[23] G. Kresse, J. Hafner, Phys. Rev. B 47 (1993) 558–561.
[24] G. Kresse, J. Furthmuller, Phys. Rev. B 54 (1996) 11169–11186.
[25] P.E. Blochl, Phys. Rev. B 50 (1994) 17953–17979.

[26] G. Kresse, D. Joubert, Phys. Rev. B 59 (1999) 1758–1775.
[27] J.P. Perdew, J.A. Chevary, S.H. Vosko, K.A. Jackson, M.R. Pederson, D.J. Singh, C. Fiolhais, Phys. Rev. B 46 (1992) 6671–6687.
[28] S.H. Vosko, L. Wilk, M. Nusair, Can. J. Phys. 58 (1980) 1200–1211.
[29] P. Olsson, C. Domain, J. Wallenius, Phys. Rev. B 75 (2007) 014110.
[30] A.V. Barashev, A.C. Arokiam, Philos. Mag. Lett. 86 (2006) 321–332.
[31] C. Becquart, J. Raulot, G. Bencteux, C. Domain, M. Perez, S. Garruchet, H. Nguyen, Comput. Mater. Sci. 40 (2007) 119–129.
[32] S. Chiesa, M.R. Gilbert, S.L. Dudarev, P.M. Derlet, H. Van Swygenhoven, Philos. Mag. 89 (2009) 3235–3243.
[33] V. Vitek, Cryst. Lattice Defects 5 (1974) 1–34.
[34] T. Klaver, R. Drautz, M. Finnis, Phys. Rev. B 75 (2006) 094435.
[35] J. Chojcan, J. Alloys Compd. 264 (1998) 50–53.
[36] V.T. Witusiewicz, F. Sommer, E.J. Mittemeijer, J. Phase Equilib. Diffus. 25 (2004) 346–354.
[37] E. Vincent, C. Becquart, C. Domain, J. Nucl. Mater. 351 (2006) 88–99.
[38] J. Chojcan, Hyperfine Interact. 156 (2004) 523–529.
[39] Y. Nagai, K. Takadate, Z. Tang, H. Ohkubo, H. Sunaga, H. Takizawa, M. Hasegawa, Phys. Rev. B 67 (2003) 224202.
[40] A. Moslang, E. Albert, E. Recknagel, A. Weidinger, P. Moser, Hyperfine Interact. 15 (1983) 409–412.
[41] F. Maury, A. Lucasson, P. Lucasson, Y. Loreaux, P. Moser, J. Phys.F-Met. Phys. 16 (1986) 523–541.
[42] H. Abe, E. Kuramoto, J. Nucl. Mater. 271–272 (1999) 209–213.
[43] F. Maury, A. Lucasson, P. Lucasson, P. Moser, Y. Loreaux, J. Phys.F-Met. Phys. 15 (1985) 1465–1484.